SSRG International Journal of Mechanical Engineering
ISSN: 2348-8360/ https://doi.org/10.14445/23488360/IJME-V11I7P109

Volume 11 Issue 7, 98-118, July 2024

Original Article

Aerodynamic Assessment of Flying Wing UAV and Impact of Dimples on its Performance

Sanket V. Kalgutkar[1], P. Booma Devi[2]

[1,2]*Department of Aeronautical, Faculty of Engineering, Sathyabama Institute of Science and Technology, Tamilnadu, India.*
[1]*Indian Institute of Tropical Meteorology, Ministry of Earth Sciences, Maharashtra, India.*

[1]*Corresponding Author : sanketvk08@gmail.com*

Received: 14 May 2024 Revised: 18 June 2024 Accepted: 17 July 2024 Published: 30 July 2024

Abstract *- Unmanned Aerial Vehicles (UAVs) stand out as of late because of their different applications in observation, ethereal planning, and information assortment. Aerodynamic productivity is pivotal in boosting UAV execution, especially for flying wing setups. One promising way to improve aerodynamic performance is using dimples on the UAV's wing surface, which alters the flow behavior and diminishes drag. This study plans to examine the effect of different dimple shapes on the aerodynamic characteristics of a flying wing UAV. This paper conducts a comprehensive numerical analysis using Computational Fluid Dynamics (CFD) simulations. The flying wing UAV model is exposed to various dimple arrangements, including round, square, and octagon shapes, put decisively along the wing surface. The CFD simulations utilize the SST k-w turbulence model to capture the flow features accurately. The aerodynamic assessment of each dimple shape is assessed by inspecting essential boundaries like lift coefficient, drag coefficient, and the coefficient of moment for UAV. Preliminary results indicate that dimples significantly affect the aerodynamic behavior of the flying wing UAV. Dimple shape prominently affects drag decrease, stream strength, and, by and large, lift-to-drag ratio. A similar examination gives experiences into the benefits and burdens related to various dimple shapes, aiding the plan streamlining process for flying wing UAVs. The optimized dimple shape recognized through this exploration might upgrade the UAV's endurance, range, and payload limit, making it a resource in applications requiring delayed or broadened flight activities.*

Keywords *- Flying wing, UAV, CFD, Dimples, Aerodynamic.*

1. Introduction

Unmanned Aerial Vehicles (UAVs) have upset the field of flight, empowering many applications across different industries. The flying wing design has acquired critical consideration among the different UAV designs because of its unique aerodynamic qualities and functional benefits. Flying wing UAVs, characterized by their absence of a distinct fuselage and tail assembly, present an intriguing platform for research and development in unmanned aerial systems.

The absence of a conventional fuselage and tail section reduces aerodynamic drag and weight, improving fuel efficiency, increased endurance, and higher payload capabilities. One of the significant advantages of flying wing UAVs is their inherent stability. The shortfall of a tail segment wipes out the requirement for a different even stabilizer, simplifying the design and diminishing upkeep necessities. In addition, the wing's enormous surface region offers regular dependability, improving maneuverability, particularly in violent or gusty circumstances. These characteristics make flying wing Unmanned Aerial Vehicles (UAVs) ideal for various tasks, such as mapping, environmental monitoring, surveillance, reconnaissance, and package delivery.

Holla S [1] describes the design and CFD analysis procedure of fixed-wing UAVs. It describes how Flying Wing UAV was designed based on the requirements and the literature survey. Design philosophy begins with airfoil choice utilizing XFLR5 and making a 3D model for CFD investigation. Two models are used for CFD analysis of UAV viz k-ω and k–ε models.

Merryisha [3] has reviewed studies on the impact of surface modifiers on aircraft wings. It focuses on how these modifiers, such as dimples and vortex generators, create turbulence and vortices to improve aerodynamic characteristics.

The review discusses various types of modifiers and their effects on stalling characteristics. It emphasizes the importance of positioning and dimension of these modifiers to achieve these aerodynamic improvements. The studies include both experimental and computational analyses, highlighting the effectiveness of different modifiers in improving aircraft stability and landing efficiency.

Using CFD models, Soundharya [4] conducted exterior flow experiments over NACA 4412 airfoils both before and after changes. Dimples such as multiple inward, outward, and inward dimples were used to modify the airfoil. The angle of attack on them was examined between -15 and 15 degrees. The ideal dimple position was determined based on the pressure and velocity curves.

Using a subsonic wind tunnel, Mustak [5] investigated the impact of dimples on the NACA 4415 airfoil. An experiment conducted in a wind tunnel revealed that the airfoil's dimples on the upper surface can be used to postpone flow separation. Flow separation for airfoil without dimples is at 12 degrees, but airfoil with dimples on the upper surface has flow separation at 16 degrees. That demonstrated that dimples delay the boundary layer separation by creating more turbulence over the surface, thus reducing the wake formation.

A CFD research on the impact of dimples on the aerodynamic efficiency of an Aspect Ratio flying wing UAV is illustrated by Ramprasadh [6]. Numerous leading-edge dimpled wing designs were analyzed, and the results showed that the pressure distribution over the airfoil surface and the vortex strength increased with depth.

Mahesh [7] studied the effects of dimples on wing aerodynamic efficiency, lift, drag, critical angle of attack, and boundary layer separation. Using CFD analysis, two dimple shapes, circular and octagonal, were examined for both inward and outward conditions. The dimples were positioned at various points along the chord. Octagonal dimpled wings showed better performance than circular dimpled wings.

Livya [8] used both computational and experimental analysis over NACA 0018 airfoil wing to examine how to increase the agility of the aircraft by delaying the flow separation point at the stall and so reducing the drag by applying the dimple effect over the aircraft wing. The improvement of wing performance was studied using various dimple forms, including square, hexagon, semi-sphere, and cylinder at various velocities.

Yazik [18] studied the aerodynamic characteristics of the S5010 Airfoil, which is used for tailless planform. This airfoil was designed for flying wing aircraft and has a positive pitching moment, which comes under the category of reflex airfoil.

Many investigations are executed to study the aerodynamic enhancements on different bodies, mainly on rectangular wings, using the symmetrical shape of an airfoil. These studies were done for different shapes and sizes of dimples to study the enhancement in aerodynamic characteristics of the body. Less literature is available on the studies of dimples for wings with reflex airfoils. Reflex airfoils are commonly used in designing flying wing UAVs.

In this paper, a flying wing UAV is designed using a reflex airfoil and computational analysis is carried out on UAVs with dimples and without dimples at different angles of attack to fill the gap in existing literature.

The existing methodology is followed for computational analysis. As the model is newly designed as per the literature survey, no experimental data is available for comparison.

2. Methodology

The study measures the effect of the different shapes of dimples on flying wing UAVs. Initially literature survey for micro category UAVs is carried out. Then, based on the primary design constraint, multiple design iterations are carried out in XFLR5 to find the best-fit design constraints.

Based on the constraints, the 3D model of UAV is designed for computational analysis. Grid independent study is carried out for different sizes of mesh to finalize the meshing for further analysis.

A literature survey is carried out for different shapes and sizes of dimples to study existing methodologies and their results; further details are mentioned in later sections.

Lastly, suitable dimples are identified and used on UAVs for studying the aerodynamic characteristics with and without dimples on UAVs. The steps followed are summarised in the below flowchart (Figure 1).

2.1. UAV Design and Modelling

The design of a UAV is based on requirements and the application for which it will be used. A literature survey for micro category UAVs with Max-Take-Off Weight (MTOW)less than and equal to 2 Kg, as shown in Table 1, is done to finalize the design requirements.

The list of UAVs shown in Table 1 is minimal, as many flying wing UAVs were considered during the literature survey.

Based on the literature survey, primary design constraints were defined for the conceptual design of flying wing UAVs. Further, multiple design iterations were performed in XFLR5 for the identified range of design constraints to arrive at best-fit design constraints, as mentioned in Table 2. A reflex airfoil, "S5010", based on a literature survey.

A three-dimensional model was created for computational analysis based on the design restrictions. The fuselage's width of 70 mm is thought to be sufficient for carrying the bare minimum of avionics and payload for operations, and its aerodynamic design reduces drag. Figure 1 displays the flying wing UAV's 3D model with a surface area of 0.44 m^2.

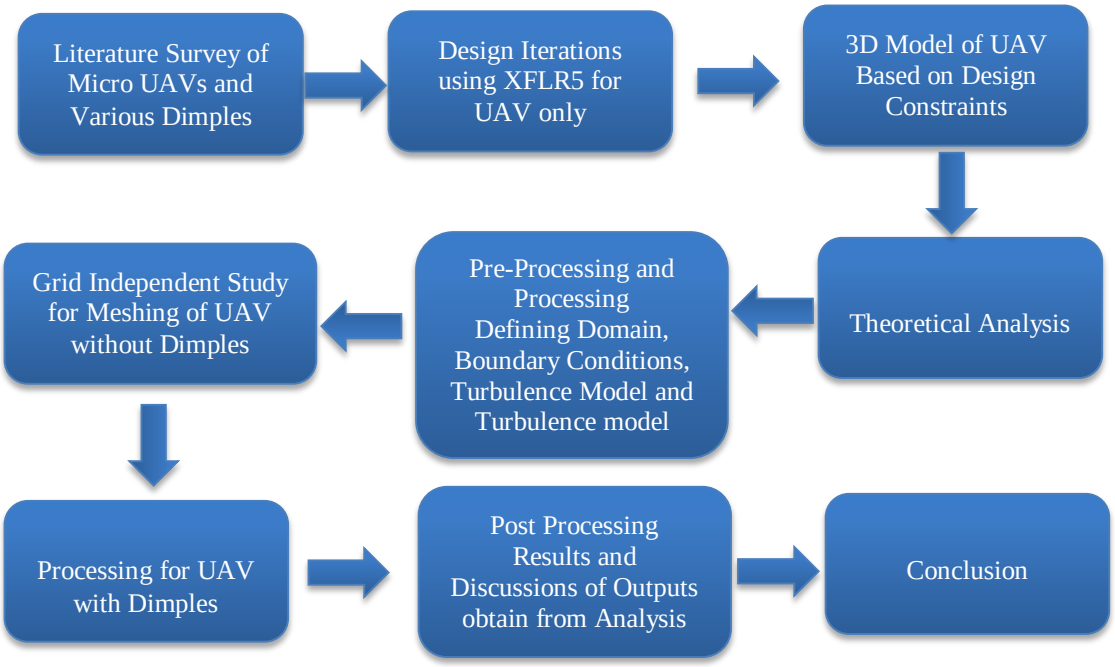

Fig. 1 Flow Chart

Table 1. Literature review for micro category UAV

UAV	Range (km)	Average Speed (m/s)	Wingspan (cm)	Mass (kg)	Endurance (min)
AHAN_EHL2	19	10	180	2	60
Delair UX11 Ag	15	47	110	1.6	52
Baaz Flying	13.3	7	96	0.69	30
Carcara	16.66	5	160	1.8	60
Micro B	16.66	10	95	1	60
Delair UX11	15	53	110	1.5	59
eBee SQ	20.5	8	110	1.1	55

Table 2. Design constraints

MTOW	2 kg
Wingspan	140 cm
Aspect Ratio	4.91
Taper Ratio	0.4255
Root Chord	400 mm
Tip Chord	170 mm
Wing Area	3990 cm^2
Root-Tip Sweep Angle	21.98°

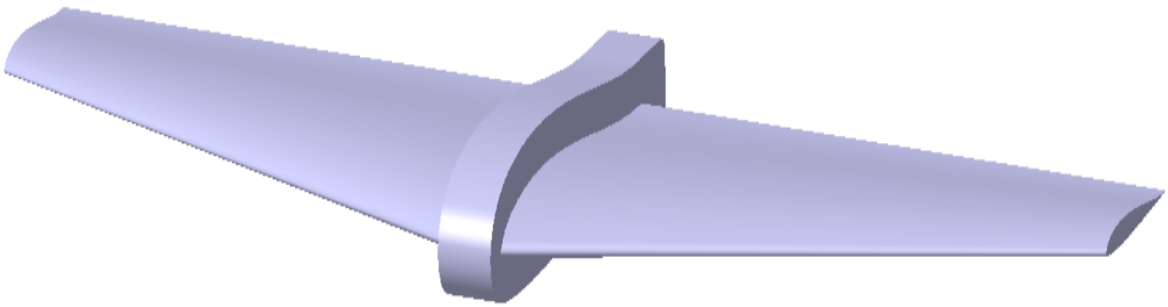

Fig. 2 3D model of UAV

2.2. Dimples Design and Modelling

A dimple is an insignificant indentation in a surface that can form both an outward and an inward dimple. Dimples can take on a variety of forms. The performance of UAVs can be greatly impacted by various dimple types and shapes, such as square, octagonal, and semi-sphere, which can enhance the stall angle of attack, decrease drag, and improve aerodynamic efficiency. Other essential characteristics are the location, size, dimensions, and distance between dimples.

Since dimples are also called vortex generators, they serve as a transition point on an airfoil by delaying the separation of the boundary layer. According to Andrei Vladimir Popov's definition [9], the airfoil transition point is situated on the upper surface and ranges from 7 to 80% of the airfoil chord. Sujit Roy [10] produced four versions of the modified airfoil for wind turbines by varying the dimple diameter from 1% to 6% of the chord length (0.01C-0.06C). For a heavily loaded compressor cascade, Wang [11] examined the Depth-to-Diameter ratio of dimples ranging from 0.125 to 0.875.

According to the survey, dimples of varying sizes and depths-to-diameter ratios were tested at various points along the chord, and computational analysis was carried out to determine the maximum Cl/Cd angle of attack for the airfoil. The following combinations of the various groupings of the parameters yield the best results: dimples with a diameter of 14 mm and a depth-to-diameter ratio of 0.5 are located on the upper surface at 50% of the root chord. There were six dimples in all, spaced 70 mm apart because an increase in the dimples did not significantly affect the results. Figure 3 depicts the inward dimples for sphere, square, and octagonal shapes, and Figure 4 outward dimples for sphere, square, and octagonal shapes on the UAV.

The models depicted in Figures 2, 3, and 4 will be employed for the computational examination of UAVs, both with and without dimples.

2.3. Lift Curve Approximation

Abbot [19] has an equation for the angle of zero lift of the wing, which is given as follows

$$\alpha_{CL=0} = \alpha_{Cl=0} + J * \varepsilon \quad (1)$$

J is a factor for determining the AOA from the chart, and ε is the twist angle, which is zero. Factor J is given by the intersection of the aspect ratio with the taper ratio. However, it is zero since ε = 0.

$$\alpha_{CL=0} = \alpha_{Cl=0} = -1°$$

As the section of the wing slope curve is linear, Abbot [19] established the following mathematical model to graph the curve.

$$C_{L\alpha} = (a * \alpha) + C_{L\alpha=0} \quad (2)$$

The equation for the airfoil slope curve of S5010 is given as follows,

$$a_0 = \frac{dC_l}{d\alpha} = \frac{C_{l\,\alpha=10^\circ} - C_{l\,\alpha=-1^\circ}}{10^\circ-(-1^\circ)} = \frac{0.32}{11} = 0.0290 \quad (3)$$

The equation for the wing slope curve is given as follows,

$$a = \frac{a_e}{1+\frac{57.3*a_e}{\pi*AR}} \quad (4)$$

$$a_e = \frac{a_0}{E} = \frac{a_0}{\frac{Wing\ Perimeter}{2b}} = \frac{0.0290}{\frac{0.399}{2.8}} = 0.2035$$

$$a = \frac{0.2035}{1 + \frac{57.3 * 0.2035}{\pi * 4.91}} = 0.1158$$

Using Equation (2),

$$0 = (0.1158) * (-1°) + C_{L\alpha=0}$$

$$C_{L\alpha=0} = 0.1158$$

So, the mathematical model to graph the wing slope curve is as follows,

$$C_L = (0.1158) * \alpha + 0.1158 \quad (5)$$

For S5010 airfoil at 0-degree AOA, Cd0 = 0.0045,

$$C_D = C_{d0} + C_{Di} \quad (6)$$

$$C_{Di} = \frac{C_L^2}{\pi ARe} \quad (7)$$

$$e = \frac{1}{(1+AR*\beta)} \quad (8)$$

β is the taper ratio, which is the ratio of the tip chord to the root chord.

$$C_{Di} = \frac{0.1158^2}{\pi * 4.91 * 0.8468} = 0.001026$$

$$C_D = 0.0045 + 0.001026 = 0.005266$$

The equation for estimating the drag coefficient is as follows,

$$C_D = 0.0045 + \frac{{C_L}^2}{13.062} \quad (9)$$

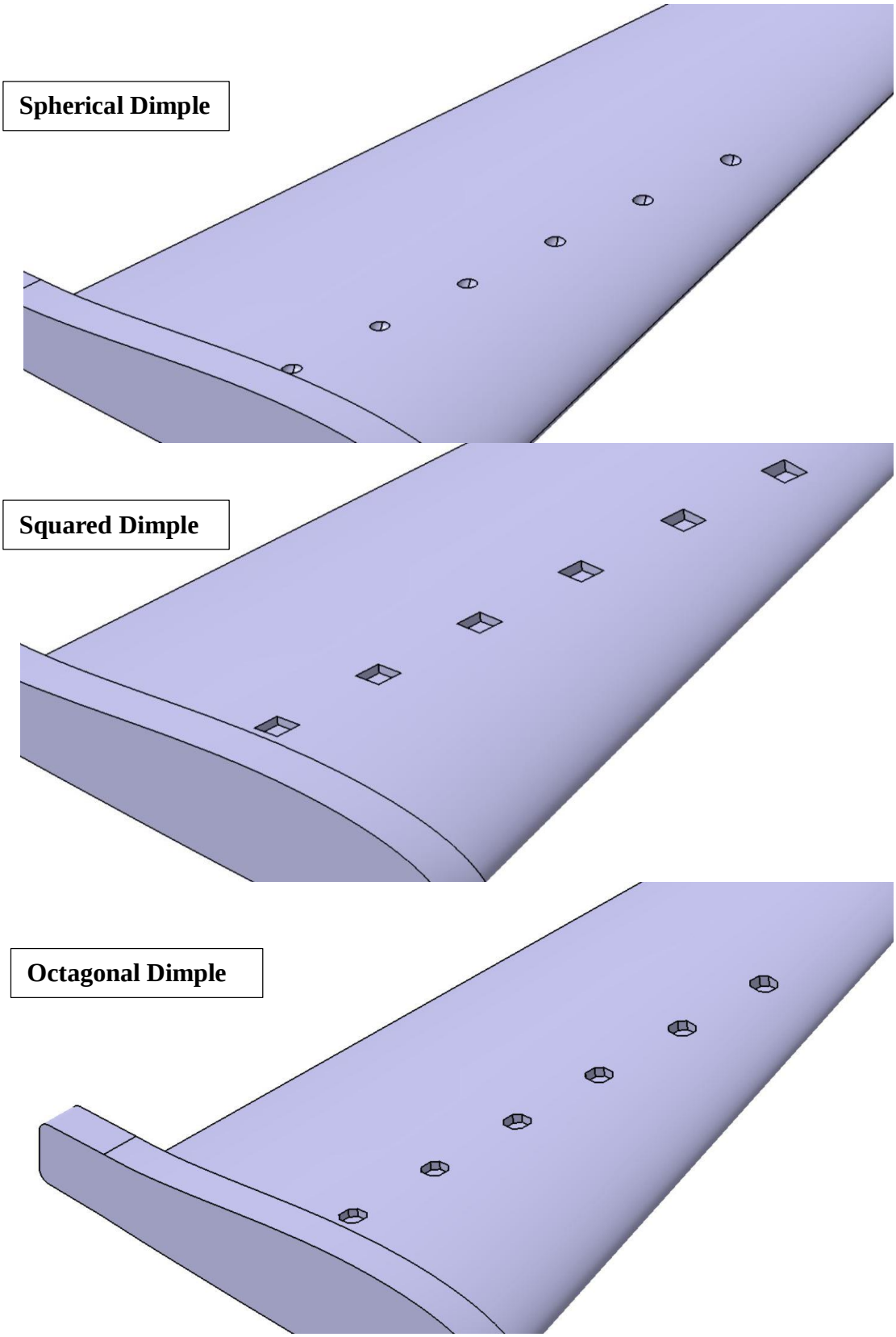

Fig. 3 Inward dimples for sphere, square, and octagonal shapes on UAV

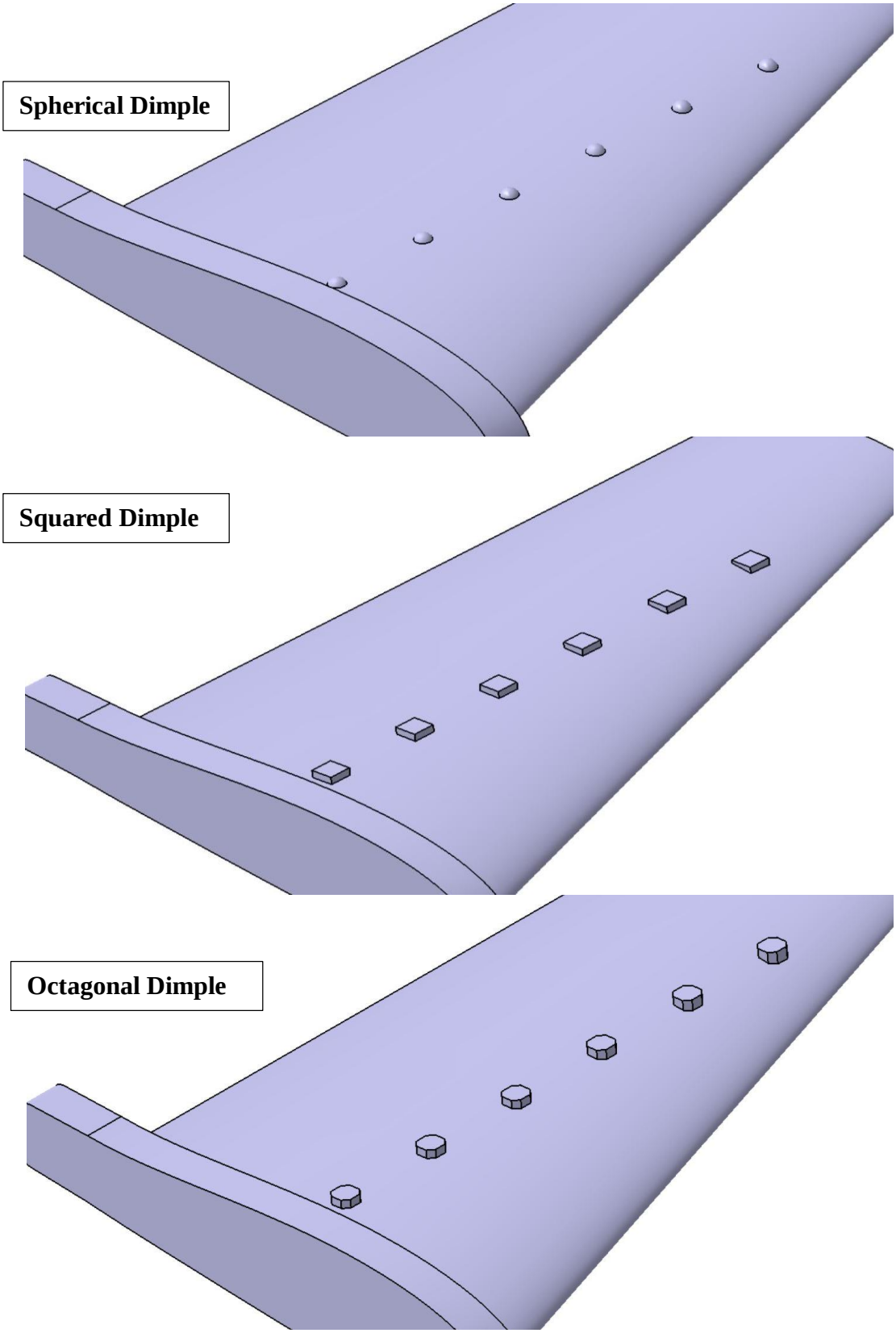

Fig. 4 Outward dimples for sphere, square, and octagonal shapes on UAV

3. Computational Analysis

3.1. Domain Detail

Figures 5 and 6 show the schematic of the rectangular domain used for the analysis of UAVs. The domain has four sides: inlet, outlet, walls, and symmetry. Symmetry is taken along the longitudinal axis of the UAV, which helps in the reduction of computation time. A sphere of influence is defined to make dense mesh near the UAV so the number of elements can be reduced. The inlet was kept at a 6C distance from the leading edge of the UAV, and the outlet was kept at 11C. The fluid domain above and below the UAV was kept at a 6C distance to avoid a wall effect on the flow around the UAV. The thickness of the domain is also kept at 6C.

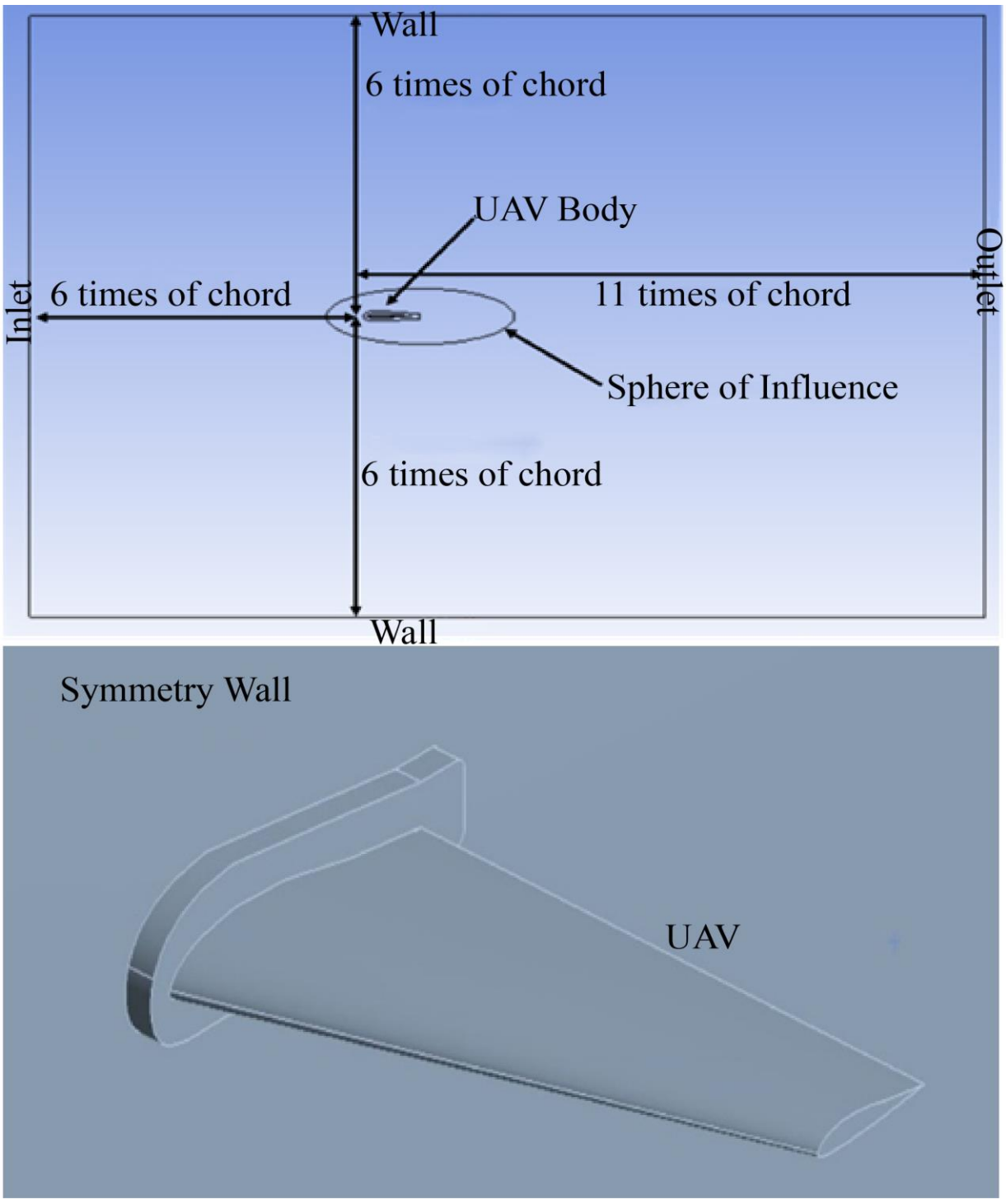

Fig. 5 Domain for UAV analysis

Unstructured meshing ensures that the same scheme and mesh quality are maintained throughout all UAV models at various angles of attack. As depicted in Figure 7, the sphere of influence and edge sizing are utilized for fine mesh in the elliptical zone around the UAV.

As seen in Figure 7, inflation is used to record the airfoil near flow field behaviour. Both dimpled and smooth UAVs mesh with the same domain, influence sphere, and inflation layer for varying attack angles. Less than 5,10,000 nodes are estimated to exist under all circumstances, with an average skewness of 0.24 and an average orthogonal quality of 0.75. Once a high-quality mesh has been achieved, the mesh is translated for additional fluid flow analysis processing.

3.2. Boundary Conditions

The standard default settings of pressure, density, and kinematic viscosity were employed in the simulation, with P = 101.3 kPa, ρ = 1.225 kg/m^3, and ν = 1.79 × 10^{-5} kg/m-s, respectively [12].

The default standard values for the input velocity, turbulence intensity, and turbulence viscosity ratio are 17 m/s, 5%, and 10%, respectively. The UAV's pressure outlet is located at the rear of the vehicle. Since the Reynolds number is smaller than 4.6 x 10^5, incompressible flow is assumed, and a pressure-based solver is used.

3.3. Turbulence Model

A mathematical model called a turbulence model is used to forecast the effects of turbulence. The most famous two-equation model CFD uses to predict mean flow features for turbulent flow conditions is the k–omega (k–ω) turbulence model, created by Wilcox [13]. It consists of two Partial Differential Equations (PDE) for two variables, k and ω, namely turbulent kinetic energy and specific dissipation rate. The model is suitable for usage for walls through the viscous sub-layer since it uses a k-ω model in the inner regions of the boundary layer. Two versions of the k-ω model are available: the Shear-Stress Transport (SST) k-ω model and the standard k-ω model [14]. Thus, a Low-Reynolds turbulence model can be derived from the SST k-ω model.

3.4. Solution Methods

Semi-Implicit Method for Pressure Implicit Method for Pressure-Linked Equations (SIMPLE) algorithm [15] in pressure-velocity coupling scheme is used in solution methods. Second-order discretization is used for pressure, momentum, turbulent dissipation energy, and turbulent dissipation rate. The convergence criteria are set to 1 x 10^{-5} for high precision results of coefficient of lift and drag. The solution is initialized using the hybrid initialization method. The procedure described above in the methodology section will be followed for UAVs with and without dimples and different angles of attack.

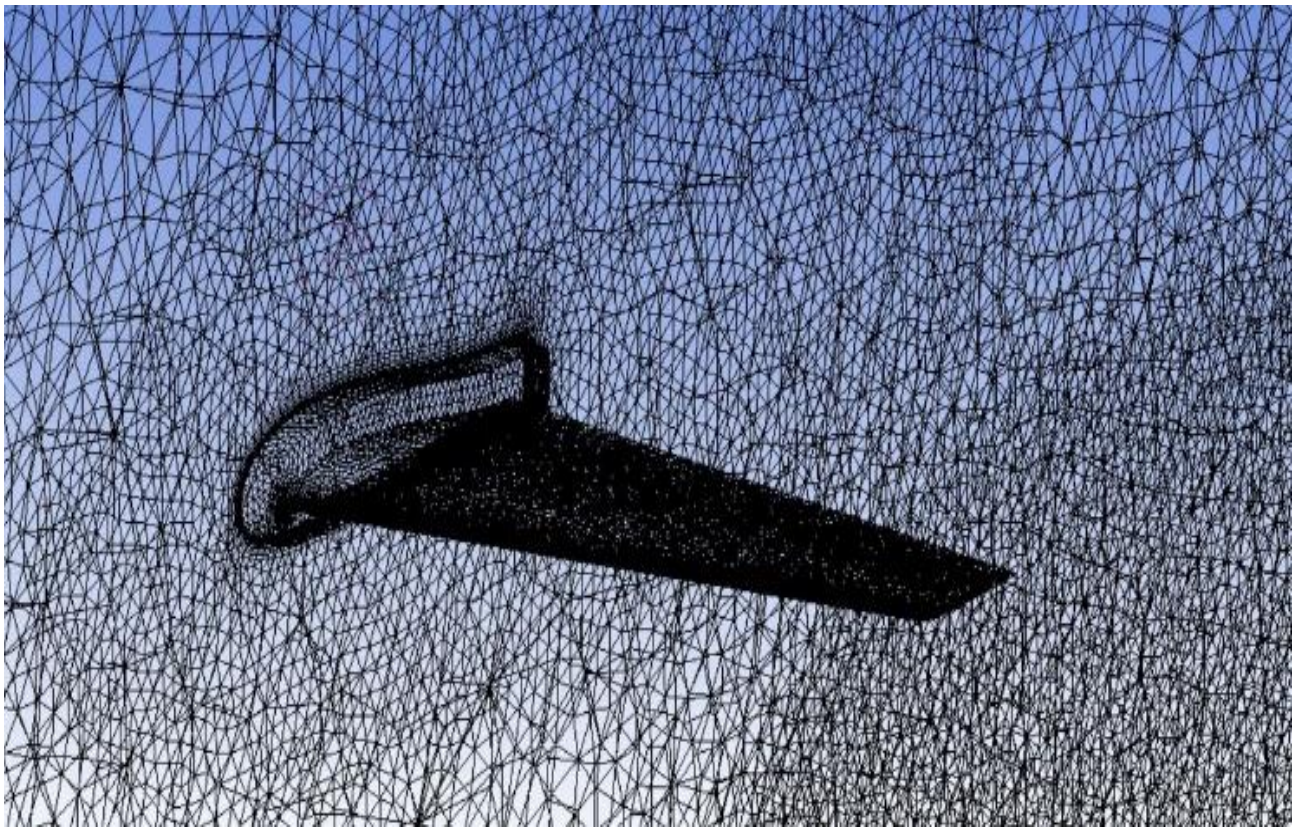

Fig. 6 Meshing on UAV (Wireframe mode)

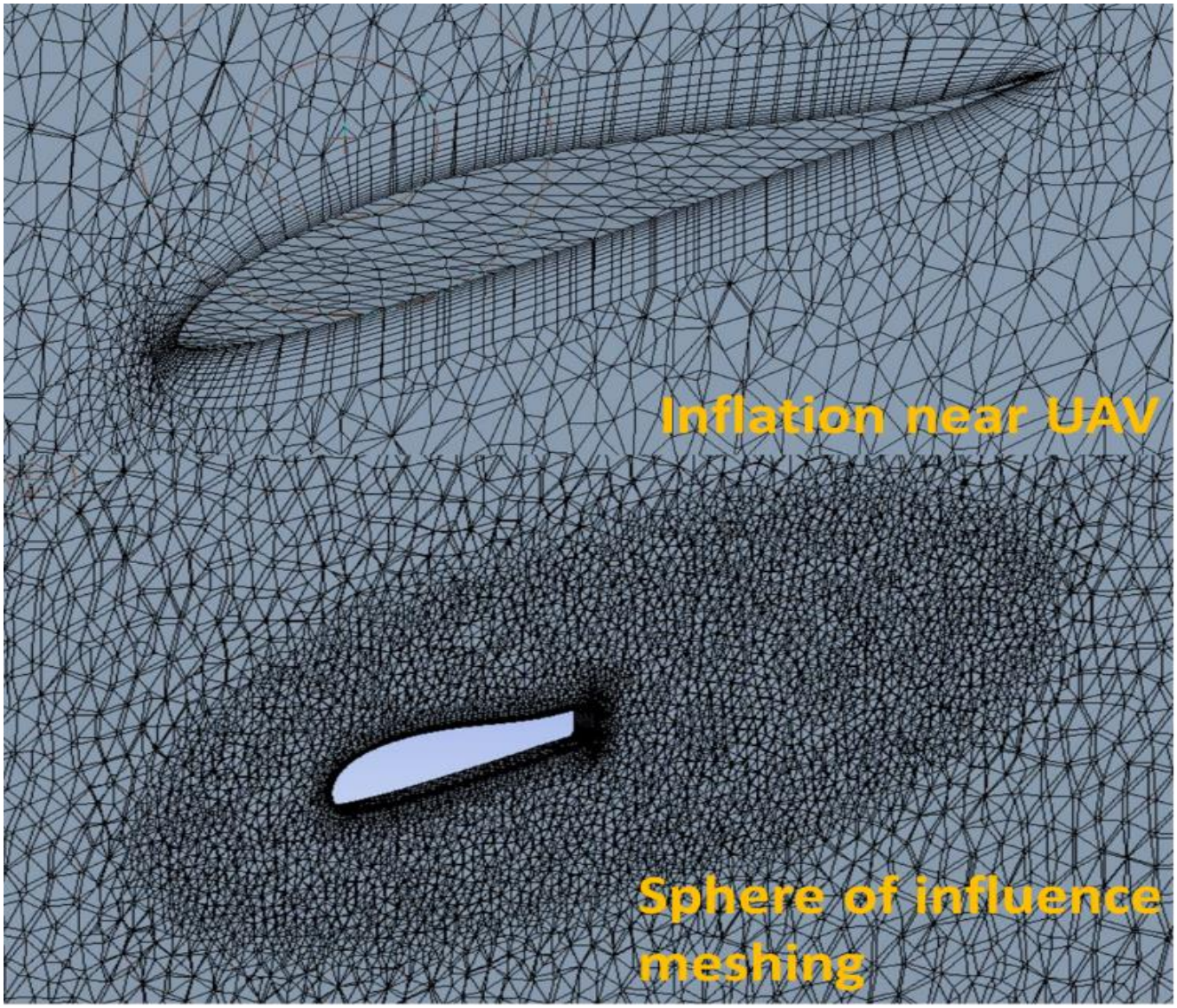

Fig. 7 Meshing on UAV with inflation and sphere of influence

3.5. Grid Independency Test

Grid Independency test is performed on UAV without dimples for different AOA. Meshing is done in 3 modes: coarse, medium, and refined, with a mesh refinement ratio of greater than 1.3 [17]. The Mesh Refinement Ratio for medium/coarse is 1.65, and the Mesh Refinement Ratio for fine/medium = is 1.38. As there is not much significant improvement observed in medium and fine mode mesh, the medium mode mesh is used in this study to reduce the computational effort. Lift, Drag, and Lift Drag ratio variation against the Angle Of Attack (AOA) for UAV with all three modes of mesh is displayed in Figures 8(a), (b), and (c).

Further results obtained by using Equations (5) and (9) are also used for reference purposes. All the curves have the same trend. Lift and drag at lower AOA has less difference when compared to higher AOA. But, the lift-to-drag ratio has less difference at higher AOA.

3.6. Other Aerodynamic Properties

Skin Friction Coefficient is a nondimensional parameter defined as the ratio of the wall shear stress and dynamic pressure.

$$C_F = \frac{\tau_w}{\rho v^2} \tag{5}$$

The quantitative indicator of the degree of turbulence for a particular flow is called Turbulent Kinetic Energy (TKE). The root mean square of the flow velocity variation can be used to quantify it [3].

$$\text{TKE} = \frac{1}{2}(u'^2 + v'^2 + w'^2) \tag{6}$$

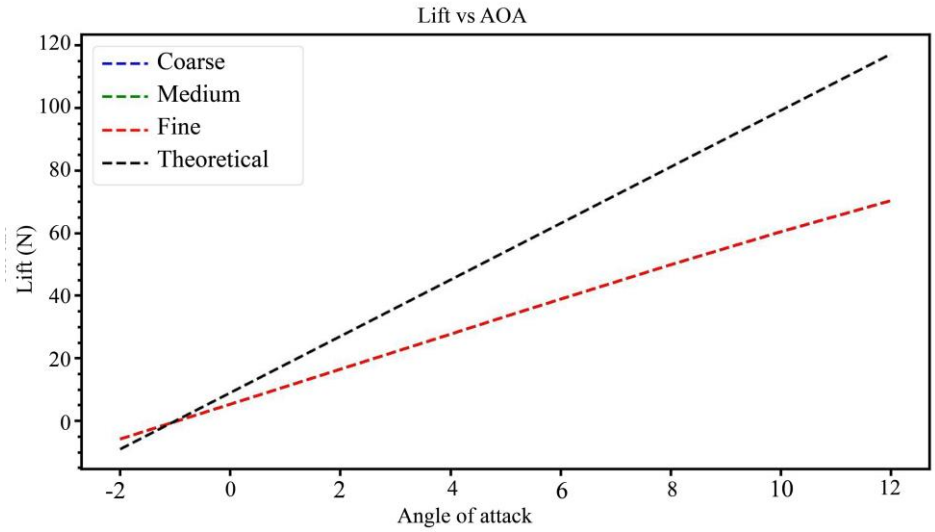

(a)

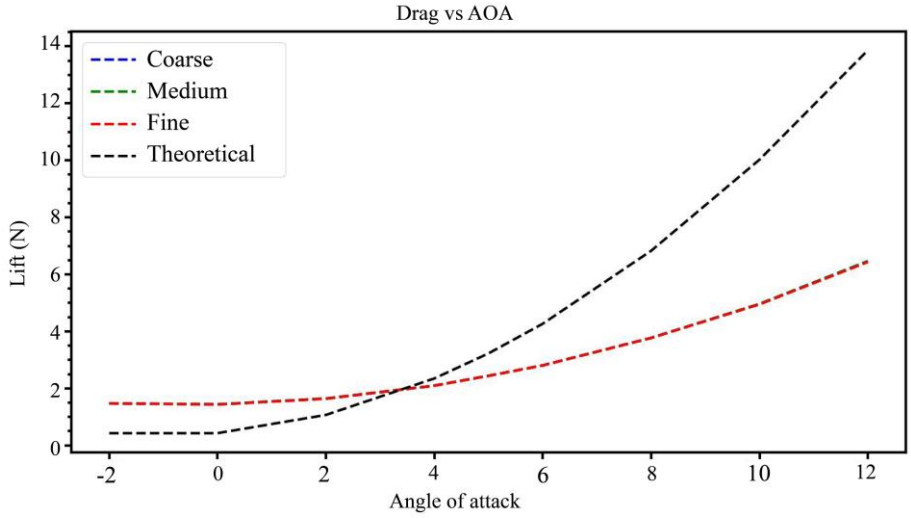

(b)

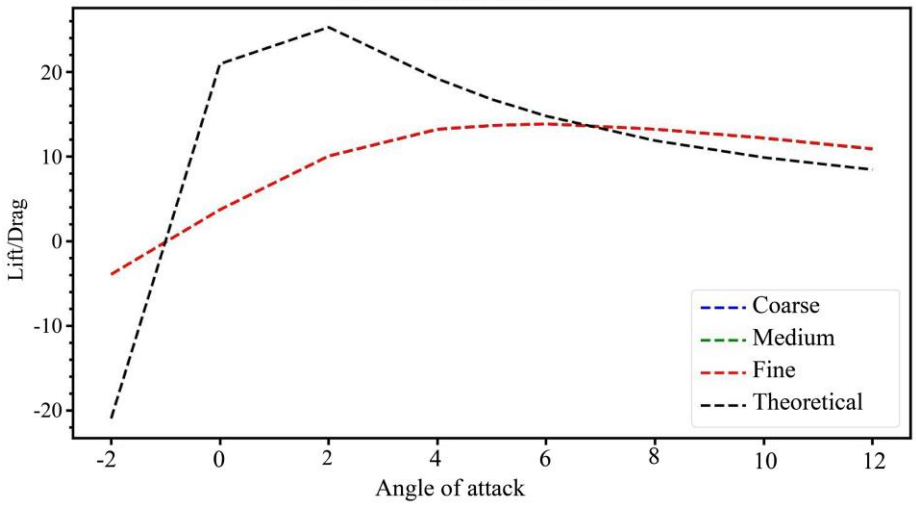

(c)

Fig. 8 Lift, drag, and lift-drag ratio vs AOA for three modes of mesh

4. Results and Discussions

4.1. Lift

Figure 9(a) shows the lift variation with AOA for inward dimple and without dimple UAV. Change in lift for different inward-shaped dimples is demonstrated in Figure 9(b). There is an increase in the lift for spherical-shaped inward dimples with an increase in AOA with a maximum increase of 0.5% at maximum AOA. Unusual behavior is observed in the case of a squared-shaped inward dimple with a change in lift between ± 0.25% with increasing AOA. There is a decrease in lift of -1.5% at 0-degree AOA with octagonal-shaped inward dimple, which is worse compared to spherical and squared-shaped inward dimple at the same AOA. Overall, the octagonal-shaped inward dimples are under-performing compared to the spherical inward dimples.

Figure 10(a) shows the lift variation with AOA for outward dimple and without dimple UAV. Change in lift for different outward-shaped dimples is demonstrated in Figure 10(b). There is a 2% increase in the lift for a squared-shaped outward dimple at 0-degree AOA, which goes on decreasing up to -12% with an increase in AOA. The spherical-shaped outward dimple starts from a drop in lift by -2% at 0-degree AOA and further remains constant with no significant change in lift and a sudden decrease to -12% after 9-degree AOA. A drop in the lift is observed in the case of octagonal-shaped outward dimples for all AOA.

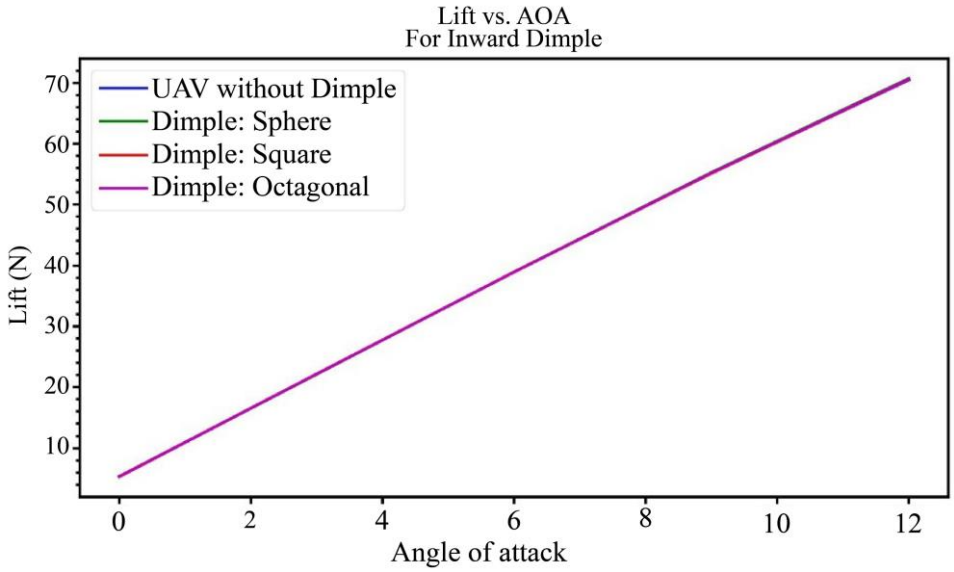

Fig. 9(a) Lift vs AOA (for inward dimples)

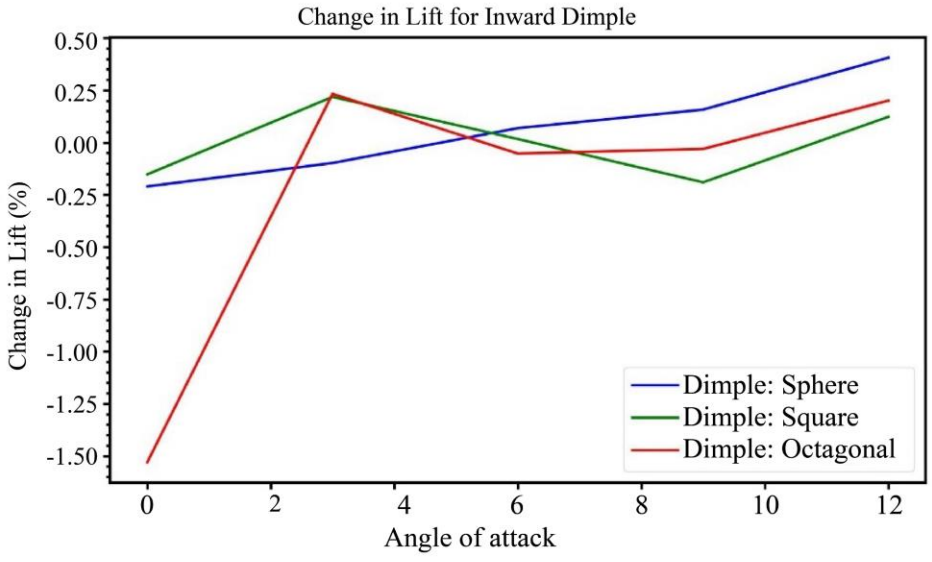

Fig. 9(b) Change in lift (%) vs AOA (for inward dimples)

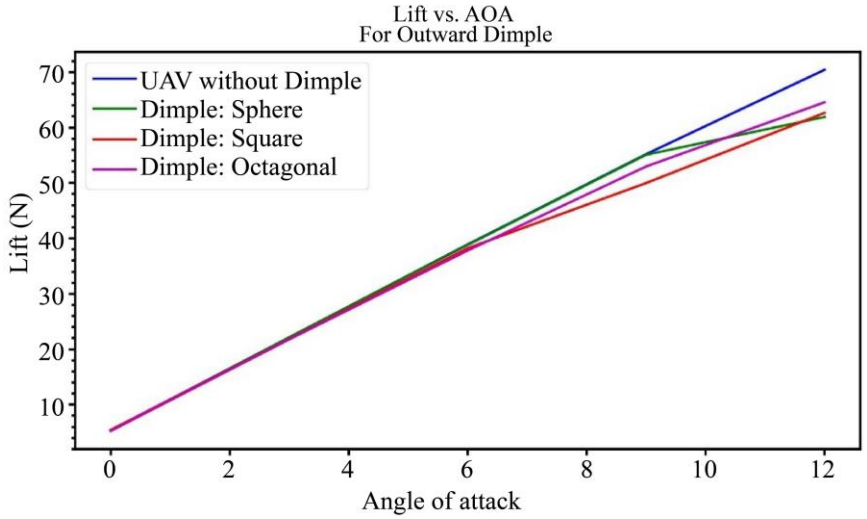

Fig. 10(a) Lift vs AOA (for outward dimples)

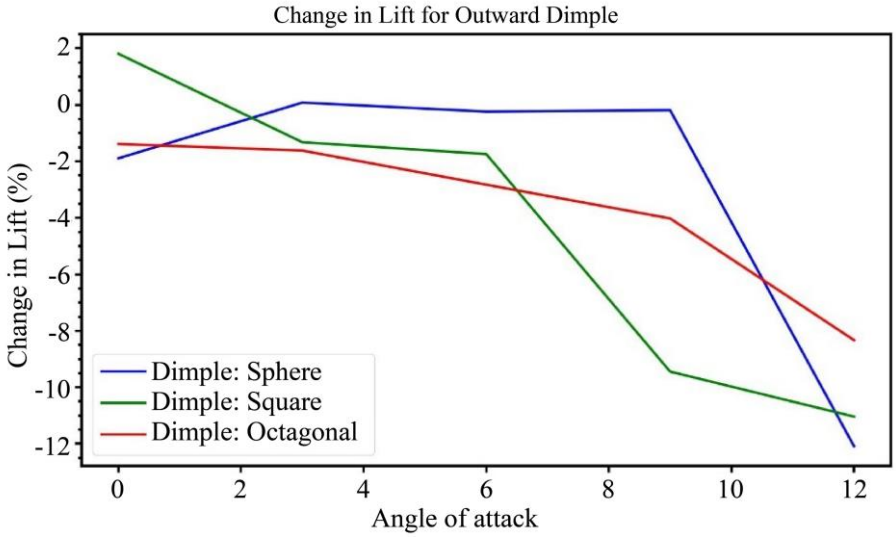

Fig. 10(b) Change in lift (%) vs AOA (for outward dimples)

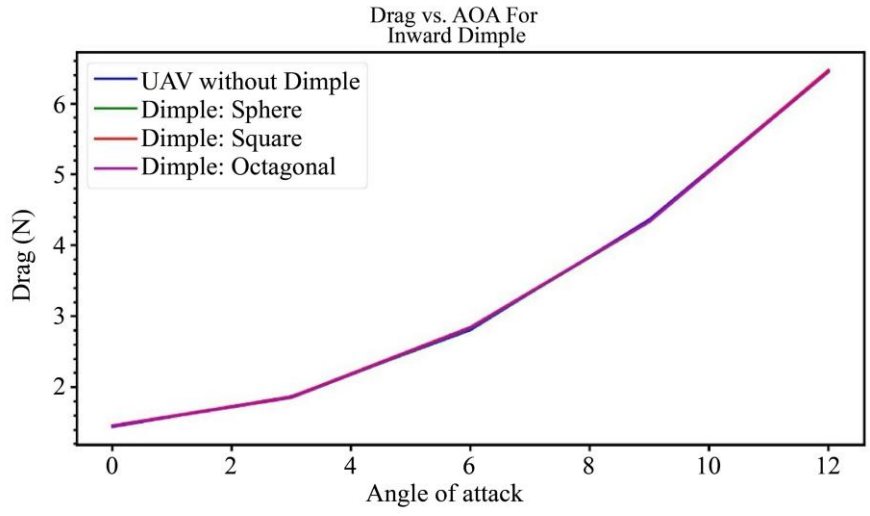

Fig. 11(a) Drag vs AOA (for inward dimples)

4.2. Drag

Figure 11(a) shows the variation of drag with AOA for inward dimple and without dimple UAV. Change in drag for different inward-shaped dimples is demonstrated in Figure 11(b). There is an increase in drag with increasing AOA, with an increase in drag of 1.5% for squared-shaped inward dimples at 0-degree and 6-degree AOA.

While for octagonal and spherical-shaped inward dimples, there is an increase in drag between 0.5 to 1 % at 0-degree and 6-degree AOA. There is a decrease in drag at 3-degree and 9-degree AOA, with a spherical-shaped inward dimple showing a drop in drag of about 1%.

Figure 12(a) shows the variation of drag with AOA for outward dimple and without dimple UAV. Change in drag for different outward-shaped dimples is demonstrated in Figure 12(b). Increase in drag for squared and octagonal-shaped outward dimples when compared to spherical-shaped outward dimples and UAVs without dimples. There is an increase in drag for spherical-shaped outward dimples, but it is significantly less compared to the other two types of dimpled UAVs.

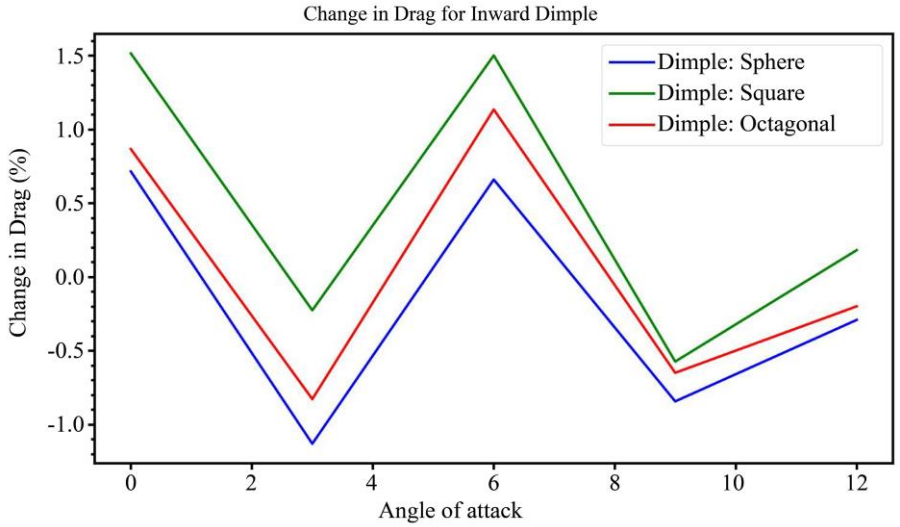

Fig. 11(b) Change in drag (%) vs AOA (for inward dimples)

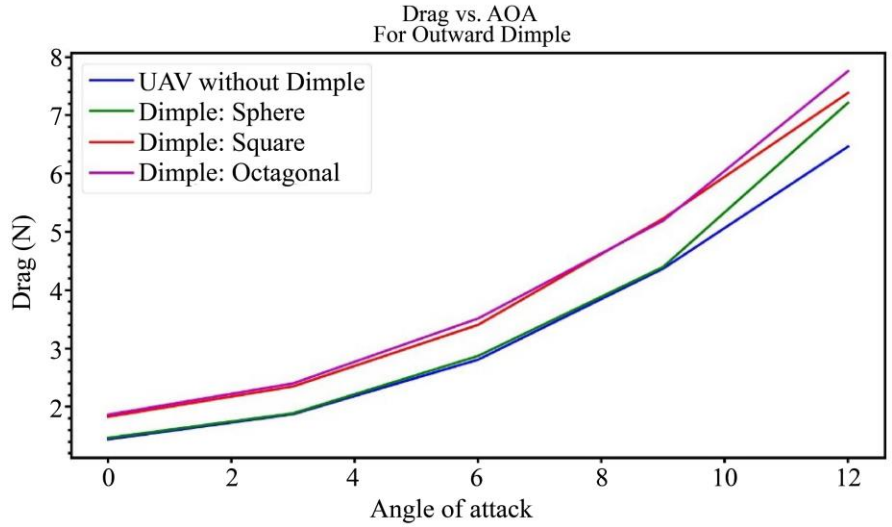

Fig. 12(a) Drag vs. AOA (for outward dimples)

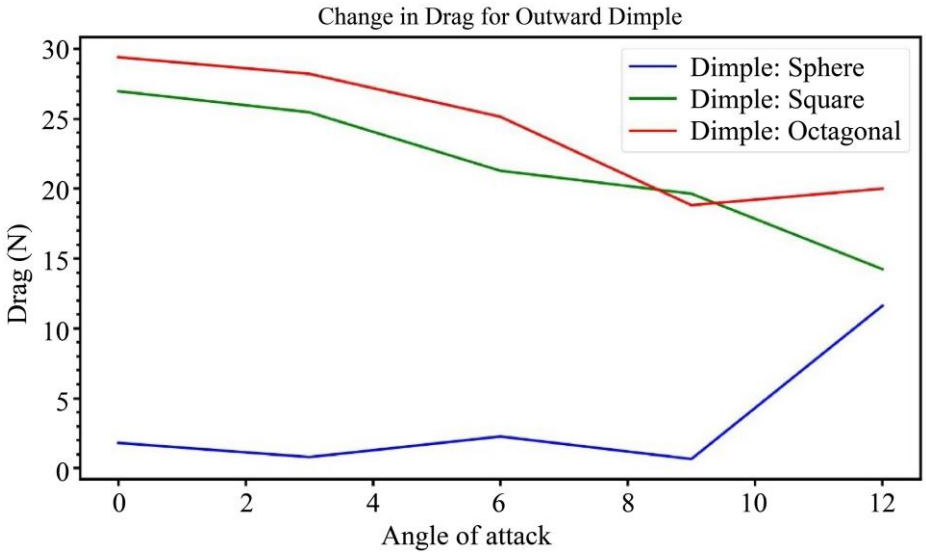

Fig. 12(b) Change in drag (%) vs AOA (for outward dimples)

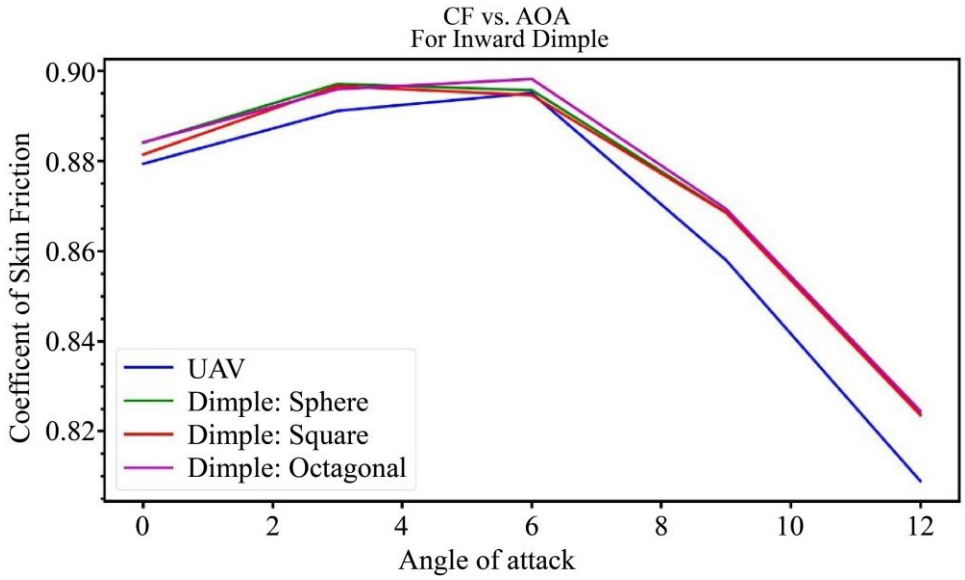

Fig. 13(a) Skin friction coefficient vs AOA (for inward dimples)

4.3. Skin Friction Coefficient

Figures 13(a) moreover, (b) shows changes in skin friction coefficient with increasing AOA for inward and outward dimple UAVs. In the case of UAV inward dimples, there is an increase in skin friction coefficient compared with UAV without dimples. For a squared-shaped outward dimple, there is a decrease in skin friction coefficient; in the case of a spherical-shaped outward dimple, there is an increase in skin friction coefficient when compared with a UAV without a dimple. There is a slight decrease in skin friction coefficient for octagonal-shaped outward dimple till 6-degree AOA when compared with UAV without dimple, but further, it increases beyond 6-degree AOA.

4.4. Turbulent Kinetic Energy

Figure 14(a) moreover, (b) shows a decrease in Turbulent Kinetic Energy (TKE) for UAVs with dimples, with the lowest for squared and octagonal-shaped inward and outward dimples compared to UAVs without dimples. Spherical inward and outward dimples are slightly more than squared and octagonal-shaped ones.

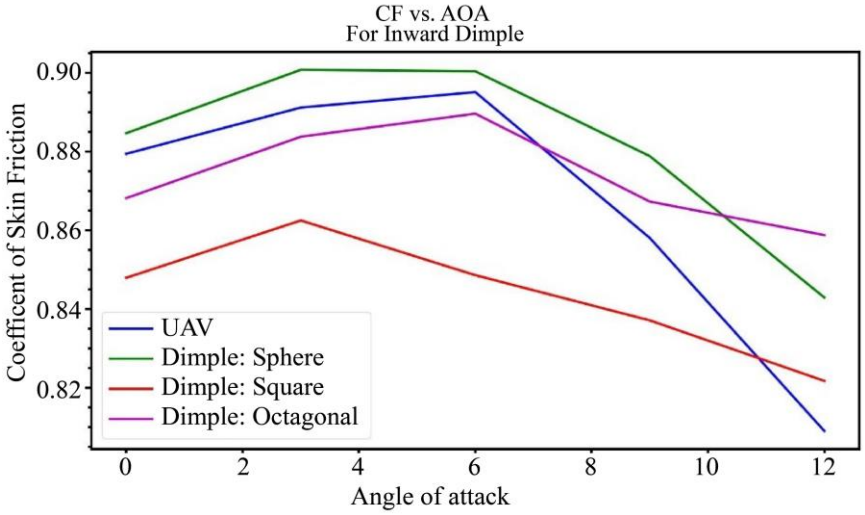

Fig. 13(b) Skin friction coefficient vs AOA (for outward dimples)

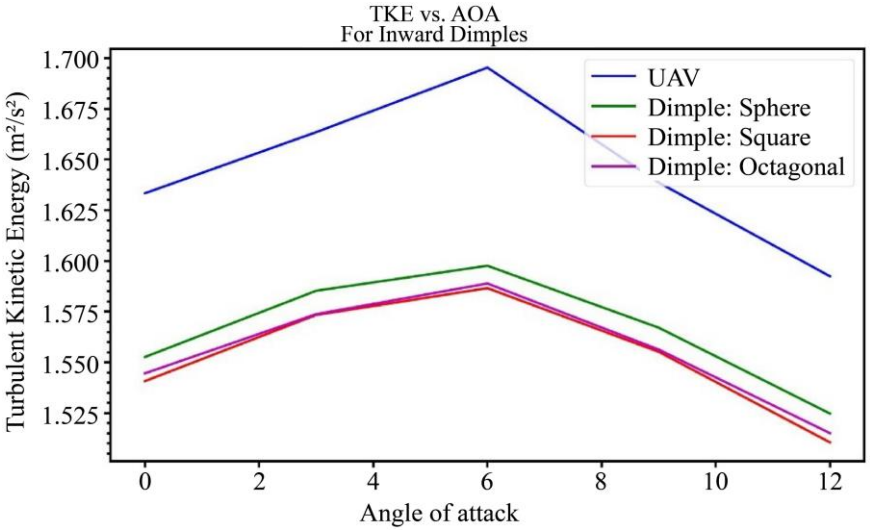

Fig. 14(a) Turbulent kinetic energy vs. AOA (for inward dimples)

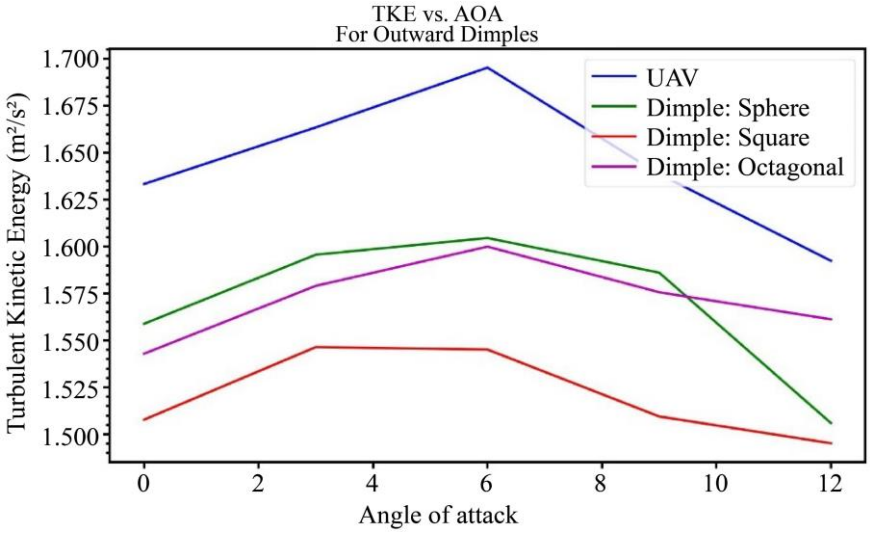

Fig. 14(b) Turbulent kinetic energy vs. AOA (for outward dimples)

4.5. Wall Shear

Lift-to-Drag ratio is maximum at 6 degrees AOA, so wall shear contours over UAV are demonstrated at 6-degree AOA. Figure 15 shows wall shear over UAV without dimples, which is maximum at the leading edge of wings and minimum at the trailing edge of wings. Figure 16 shows wall shear over UAV for spherical, squared, and octagonal-shaped inward dimples. Wall shear has an increase on the leading edge of wings for inward dimples, with maximum in case of octagonal dimples and minimum in case of UAV without dimples.

Figure 17 shows wall shear over UAV for spherical, squared, and octagonal-shaped outward dimples. Wall shear is maximum at dimples position in spherical and octagonal dimples, and in squared dimples, UAV wall shear is maximum at the wing's leading edge.

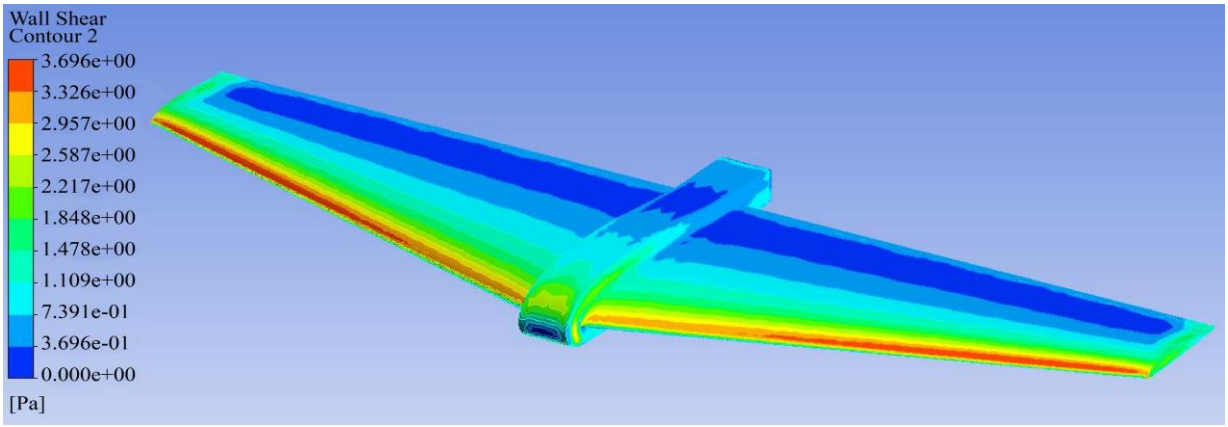

Fig. 15 Wall shear over UAV

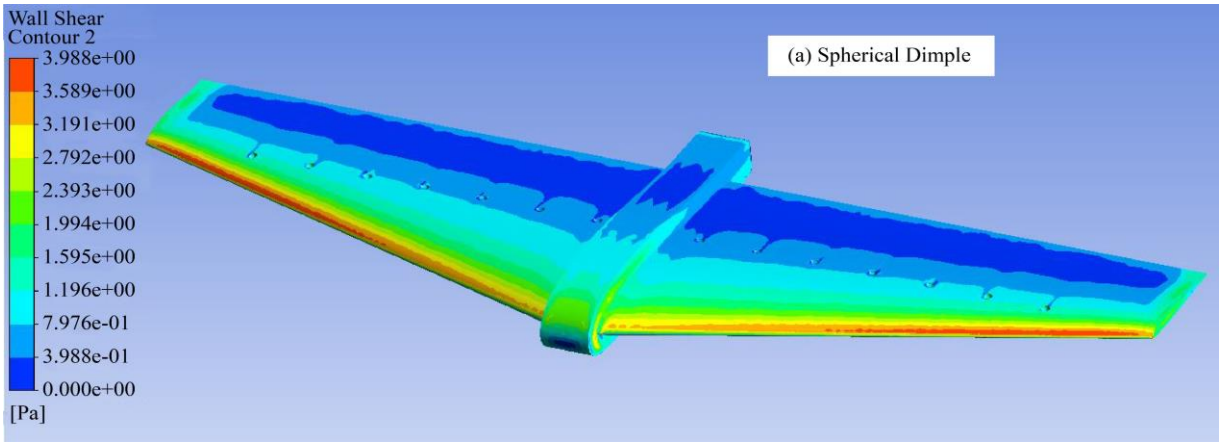

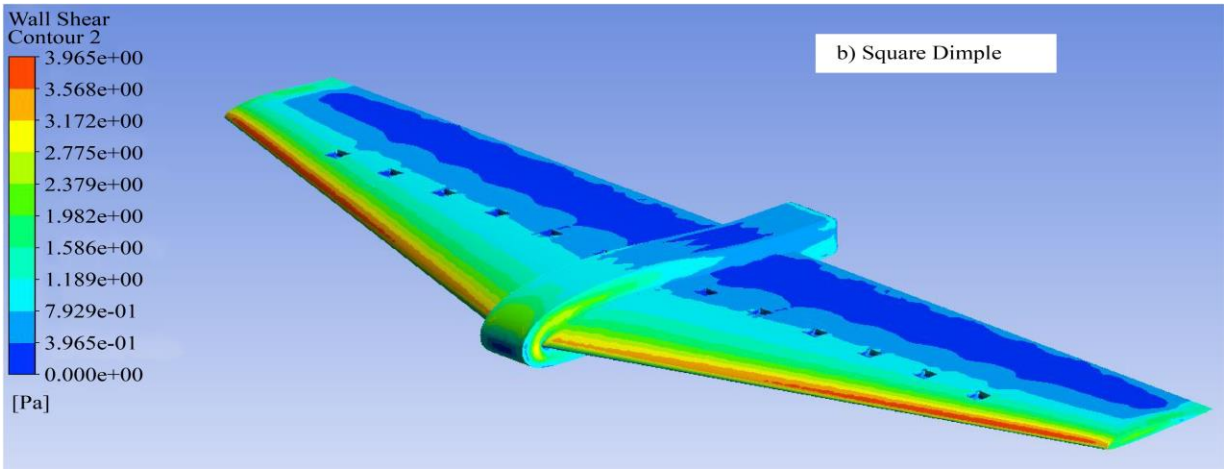

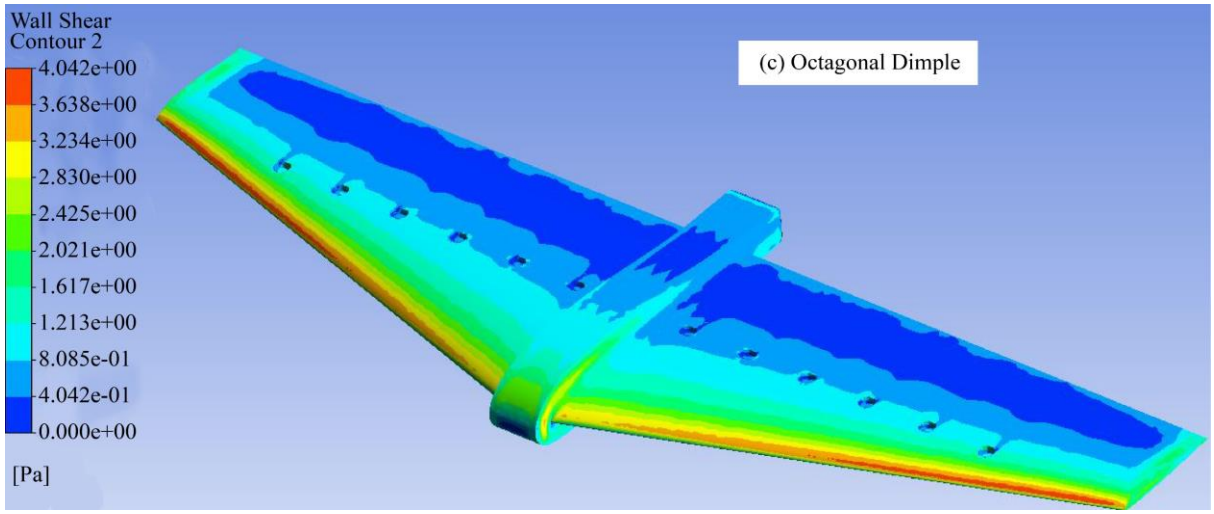

Fig. 16(a), (b), (c) For inward shape dimples

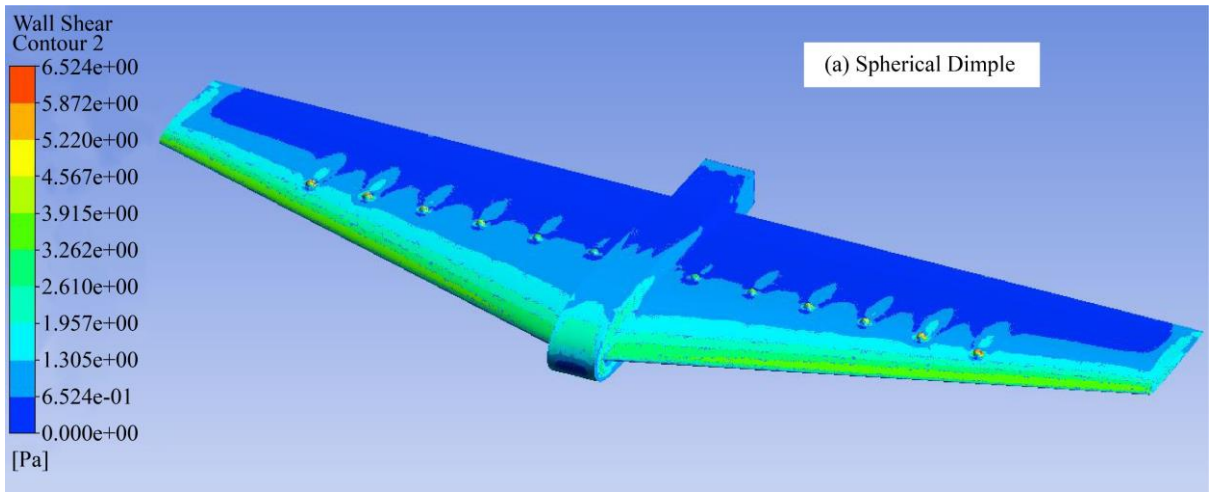

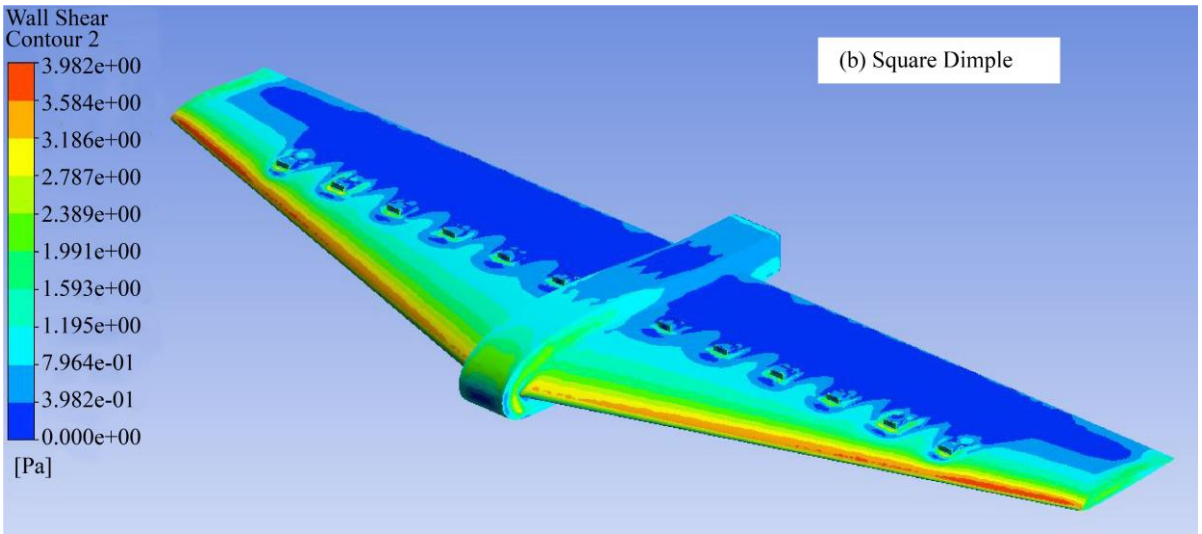

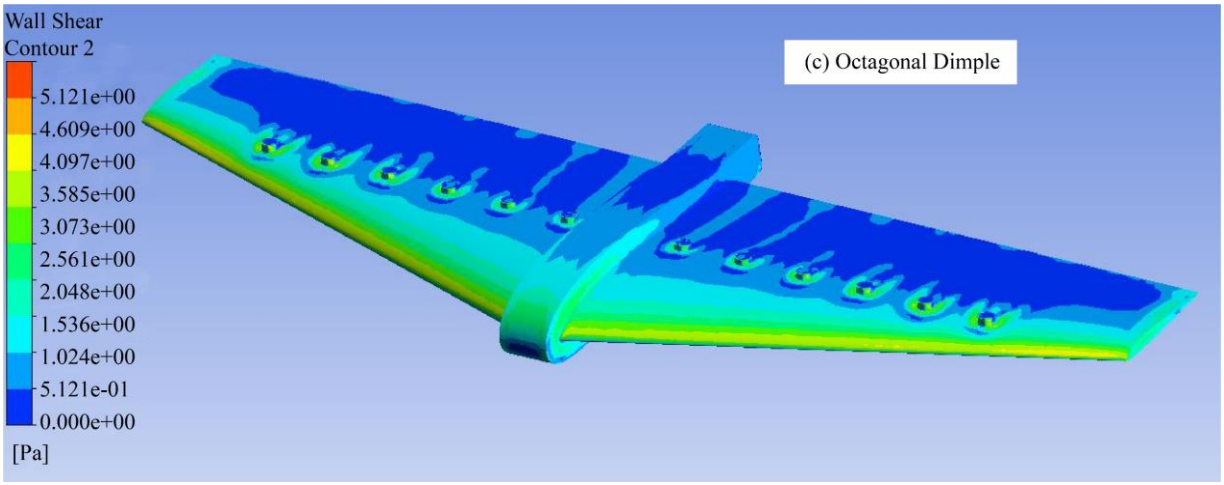

Fig. 17(a), (b), (c) For outward shape dimples

5. Conclusion

This work examines the computational analysis of UAV design both with and without dimples. Theoretical analysis was performed to estimate the lift curve slope and further to obtain the drag and lift-to-drag ratio. Theoretical analysis is not performed for dimple UAVs as a change in area is small, and it may be difficult to identify any changes using equations. Turbulent Kinetic Energy, lift, drag, and the skin friction coefficient are all calculated using the SST k-ω model. The dimple disrupts the airflow, creating mini vortices that energize the boundary layer. This helps maintain smooth airflow over the upper wing surface for a longer duration, even at high angles of attack, which also means delayed stall, increase in lift, and decrease in Drag, potentially reducing the impact of side forces and improving stability. Spherical shapes are more efficient with inner dimples than squared and octagonal shapes, as increased lift and decreased Drag are observed. Also, a slight increase in skin friction coefficient is observed with more spherical inward dimples with TKE than squared and octagonal shapes. The same is observed with outward dimples, except for more drag and skin friction coefficient increases compared to UAVs without dimples. The wall shear is maximum in the case of an outward spherical and octagonal dimple near the dimple's position at 6 degrees AOA. As very less studies are available for use on dimples over reflex airfoils wings, detailed analysis needs to be carried out using experimental analysis. Equations used in the theoretical analysis are widely used for the design of aircraft/UAVs and, hence, were used for comparison. Trend-wise, CFD and theoretical results were the same, but some differences in the values were observed. Hence, grid independent study is done for different mesh sizes to confirm consistency in results. Overall, this study suggests that a spherical inward-shaped dimple is more efficient than the other two shapes for both inward and outward dimples. Experimental studies need to be carried out for validation of these data.

Acknowledgments

The authors wish to thank monitoring committee members and Dr. Padma Kumari, a scientist at the Indian Institute of Tropical Meteorology, Ministry of Earth Sciences, Pune, for their continuous guidance and support.

References

[1] M.A. Karthik et al., "Design and CFD Analysis of a Fixed Wing for an Unmanned Aerial Vehicle," *International Journal of Latest Engineering Research and Applications*, vol. 2, no. 7, pp. 77-85, 2017. [Google Scholar] [Publisher Link]

[2] Diego Armando Mejía Bugallo et al., "Design and Aerodynamic Analysis of an Unmanned Aerial Vehicle with A Fixed-Wing," *Journal of Archaeology of Egypt/Egyptology*, vol. 19, no. 2, pp. 1-20, 2022. [Google Scholar] [Publisher Link]

[3] Samuel Merryisha, and Parvathy Rajendran, "Experimental and CFD Analysis of Surface Modifiers on Aircraft Wing: A Review," *CFD Letters*, vol. 11, no. 10, pp. 46-56, 2019. [Google Scholar] [Publisher Link]

[4] V. Soundharya et al., "Aerodynamic Analysis of Dimple Effect on Airfoil," *International Journal of Engineering and Advanced Technology*, vol. 5, no. 4, pp. 207-211, 2016. [Google Scholar] [Publisher Link]

[5] Rubiat Mustak, Nizam Uddin, and Mohammad Mashud, "Effect of Different Shaped Dimples on Airfoils," *Proceeding of the International Conference on Mechanical Engineering and Renewable Energy*, Chittagong, Bangladesh, pp. 1-4, 2015. [Google Scholar] [Publisher Link]

[6] C. Ramprasadh, and V. Devanandh, "A CFD Study on Leading Edge Wing Surface Modification of a Low Aspect Ratio Flying Wing to Improve Lift Performance," *International Journal of Micro Air Vehicles*, vol. 7, no. 3, pp. 361-373, 2015. [CrossRef] [Google Scholar] [Publisher Link]

[7] T.S. Mahesh Babu et al., "Computational Analysis of Different Shapes of Dimple on Wing," *Applied Mechanics and Materials*, vol. 766-767, pp. 1061-1069, 2015. [CrossRef] [Google Scholar] [Publisher Link]

[8] E. Livya, G. Anitha, P. Valli, "Aerodynamic Analysis of Dimple Effect on Aircraft Wing," *International Journal of Mechanical, Aerospace, Industrial, Mechatronic and Manufacturing Engineering*, vol. 9, no. 2, pp. 1-4, 2015. [Google Scholar]

[9] Andrei Vladimir Popov, Ruxandra Mihaela Botez, and Michel Labib, "Transition Point Detection from the Surface Pressure Distribution for Controller Design," *Journal of Aircraft*, vol. 45, no. 1, pp. 23-28, 2008. [CrossRef] [Google Scholar] [Publisher Link]

[10] Sujit Roy et al., "Flow Control of a Wind-Turbine Airfoil with a Leading-Edge Spherical Dimple," *International Journal of Green Energy*, vol. 20, no. 12, pp. 1307-1325, 2023. [CrossRef] [Google Scholar] [Publisher Link]

[11] Long Wang et al., "Numerical Study of the Ratio of Depth-to-Print Diameter on the Performance and Flow Characteristics for a Dimpled, Highly Loaded Compressor Cascade," *Aerospace*, vol. 9, no. 8, pp. 1-21, 2022. [CrossRef] [Google Scholar] [Publisher Link]

[12] Ira H. Abbott, Albert E. Von Doenhoff, and Louis S. Stivers, "*Summary of Low-Speed Airfoil Data*," *National Advisory Committee for Aeronautics*, NASA Technical Report, no. 824, pp. 1-261, 1945. [Google Scholar] [Publisher Link]

[13] David C. Wilcox, "Formulation of the k-ω Turbulence Model Revisited," *AIAA Journal*, vol. 46, no. 11, pp. 2823-2838, 2008. [CrossRef] [Google Scholar] [Publisher Link]

[14] David C. Wilcox, *Turbulence Modeling for CFD*, DCW Industries, Incorporated, pp. 1-460, 1993. [Google Scholar] [Publisher Link]

[15] Richard H. Pletcher, Dale Anderson, and John C. Tannehill, *Computational Fluid Mechanics and Heat Transfer*, 3rd ed., Taylor & Francis, pp. 1-753, 2013. [Google Scholar] [Publisher Link]

[16] Roger E. Bilstein, "Introduction to Flight: Its Engineering and History," *Technology and Culture*, vol. 21, no. 3, pp. 524-525, 1980. [Google Scholar] [Publisher Link]

[17] Lenonard E. Schwer, "Is your Mesh Refined Enough? Estimating Discretization Error Using GCI," *7th LS-Dyna Anwenderforum*, pp. 1-10, [Google Scholar] [Publisher Link]

[18] Muhamad Hasfanizam Mat Yazik et al., "Computational Study on Aerodynamic Characteristics and Behaviour of S5010 Airfoil," *Journal of Advanced Research in Fluid Mechanics and Thermal Sciences*, vol. 66, no. 1, pp. 42-52, 2020. [Google Scholar] [Publisher Link]

[19] Ira H. Abbott, and A.E. Von Doenhoff, *Theory of Wing Sections: Including a Summary of Airfoil Data*, Dover Publications, pp. 1-704, 2012. [Google Scholar] [Publisher Link]

Appendix 1

Table A1. Data for Figures 8(a) and (b)

AOA	Coarse	Medium	Fine	Theoretical	Coarse	Medium	Fine	Theoretical
	Lift				Drag			
-2	-5.78786	-5.77244	-5.78038	-9.0191409	1.47806	1.47744	1.4739	0.430443142
0	5.36288	5.35626	5.34286	9.0191409	1.44222	1.43948	1.436	0.430443142
2	16.54592	16.573423	16.5001366	27.0574227	1.6459	1.64652008	1.6356439	1.070110278
4	27.714642	27.70312	27.778188	45.0957045	2.0992752	2.09667	2.09624	2.34944455
5	33.37542	33.39402	33.39815	54.1148454	2.44426	2.44198	2.43941	3.228986862
6	38.899772	38.914632	38.94818	63.1339863	2.8093488	2.8067	2.80654	4.268445958
8	49.917462	49.92026	49.92026	81.1722681	3.7753028	3.76878	3.76878	6.827114501
10	60.4154	60.48214	60.48562	99.2105499	4.96176	4.96652	4.94844	10.02545018
12	70.39362	70.43314	70.39442	117.2488317	6.46814	6.46264	6.43452	13.863453

Table A2. Data for Figure 7(c)

AOA	Coarse	Medium	Fine	Theoretical
	Lift-to-Drag Ratio			
-2	-3.915849154	-3.907055447	-3.921826447	-20.95315274
0	3.71849	3.720969	3.720655	20.95315274
2	10.05281001	10.06572783	10.08785384	25.284705
4	13.20200515	13.21291381	13.25143495	19.19419826
5	13.65461121	13.67497686	13.69107694	16.75907884
6	13.84654408	13.86490612	13.87765006	14.79085993
8	13.22210817	13.24573469	13.24573469	11.88968899
10	12.17620361	12.1779717	12.22316932	9.895869822
12	10.88313178	10.89850897	10.94011985	8.45740464

Table A3. Data for Figures 9(a) and (b)

AOA	UAV	Inward-Sphere	Inward-Square	Inward-Octagonal	Change in Lift (Inward)-Sphere	Change in Lift (Inward)-Square	Change in Lift (Inward)-Octagonal
0	5.3563	5.3451	5.3481	5.2743	-0.2091	-0.1515	-1.5295
3	22.1383	22.1168	22.1869	22.1901	-0.0968	0.2195	0.2339
6	38.9146	38.9418	38.9216	38.8945	0.0699	0.0179	-0.0517
9	55.2012	55.2888	55.0967	55.1849	0.1586	-0.1894	-0.0296
12	70.4331	70.7200	70.5209	70.5753	0.4072	0.1245	0.2018

Table A4. Data for Figure 10(a) and (b)

AOA	UAV	Outward-Sphere	Outward-Square	Outward-Octagonal	Change in Lift (Outward)-Sphere	Change in Lift (Outward)-Square	Change in Lift (Outward)-Octagonal
0	5.3563	5.2549	5.4531	5.2820	-1.8923	1.8076	-1.3865
3	22.1383	22.1559	21.8455	21.7800	0.0797	-1.3226	-1.6184
6	38.9146	38.8216	38.2366	37.8147	-0.2389	-1.7425	-2.8264
9	55.2012	55.0969	49.9877	52.9809	-0.1889	-9.4445	-4.0223
12	70.4331	61.9206	62.6585	64.5661	-12.0859	-11.0383	-8.3299

Table A5. Data for Figure 11(a) and (b)

AOA	UAV	Inward-Sphere	Inward-Square	Inward-Octagonal	Change in Drag (Inward)-Sphere	Change in Drag (Inward)-Square	Change in Drag (Inward)-Octagonal
0	1.4395	1.4498	1.4613	1.4520	0.7157	1.5151	0.8670
3	1.8716	1.8505	1.8674	1.8561	-1.1289	-0.2253	-0.8266
6	2.8067	2.8252	2.8488	2.8386	0.6605	1.5015	1.1352
9	4.3677	4.3309	4.3427	4.3393	-0.8419	-0.5721	-0.6484
12	6.4626	6.4439	6.4744	6.4498	-0.2902	0.1824	-0.1981

Table A6. Data for Figures 12(a) and (b)

AOA	UAV	Outward-Sphere	Outward-Square	Outward-Octagonal	Change in Drag (Outward)-Sphere	Change in Drag (Outward)-Square	Change in Drag (Outward)-Octagonal
0	0.7197	0.7328	0.9139	0.9314	1.8116	26.9745	29.4079
3	0.9358	0.9433	1.1741	1.1999	0.7982	25.4689	28.2172
6	1.4034	1.4352	1.7020	1.7563	2.2707	21.2831	25.1475
9	2.1838	2.1982	2.6128	2.5949	0.6573	19.6446	18.8215
12	3.2313	3.6068	3.6916	3.8777	11.6193	14.2430	20.0031

Table A7. Data for Figures 13(a) and (b)

AOA	UAV	Inward-Sphere	Inward-Square	Inward-Octagonal	Outward-Sphere	Outward-Square	Outward-Octagonal
0	0.8794	0.8841	0.8815	0.8842	0.8847	0.8479	0.8681
3	0.8912	0.8972	0.8966	0.8960	0.9008	0.8625	0.8837
6	0.8951	0.8957	0.8946	0.8982	0.9004	0.8486	0.8896
9	0.8580	0.8687	0.8685	0.8694	0.8788	0.8371	0.8673
12	0.8090	0.8238	0.8236	0.8245	0.8429	0.8217	0.8588

Table A8. Data for Figures 14(a) and (b)

AOA	UAV	Inward-Sphere	Inward-Square	Inward-Octagonal	Outward-Sphere	Outward-Square	Outward-Octagonal
0	1.6334	1.5526	1.5407	1.5446	1.5589	1.5078	1.5430
3	1.6635	1.5853	1.5734	1.5738	1.5957	1.5465	1.5791
6	1.6953	1.5976	1.5866	1.5889	1.6046	1.5452	1.6000
9	1.6386	1.5671	1.5552	1.5563	1.5861	1.5095	1.5757
12	1.5924	1.5248	1.5106	1.5151	1.5061	1.4952	1.5613